Potential of next-generation imaging spectrometers to detect and quantify methane point sources from space

Daniel H. Cusworth[1,3], Daniel J. Jacob[1], Daniel J. Varon[1,4], Christopher Chan Miller[2], Xiong Liu[2], Kelly Chance[2], Andrew K. Thorpe[3], Riley M. Duren[3], Charles E. Miller[3], David R. Thompson[3], Christian Frankenberg[3,5], Luis Guanter[6], and Cynthia A. Randles[7]

[1]School of Engineering and Applied Sciences, Harvard University, Cambridge, MA, USA

[2]Atomic and Molecular Physics Division, Harvard Smithsonian Center for Astrophysics, Cambridge, MA, USA

[3]Jet Propulsion Laboratory, California Institute of Technology, Pasadena, CA, USA

[4]GHGSat, Inc., Montréal, QC H2W 1Y5, Canada

[5]Division of Geology and Planetary Sciences, California Institute of Technology, Pasadena, CA, USA

[6]Centro de Tecnologías Físicas, Universitat Politècnica de València, Camí de Vera s/n, 46022 València, Spain

[7]ExxonMobil Research and Engineering Company, Annandale, NJ, USA

Abstract

We examine the potential for global detection of methane plumes from individual point sources with the new generation of spaceborne imaging spectrometers (EnMAP, PRISMA, EMIT, SBG, CHIME) scheduled for launch in 2019-2025. These instruments are designed to map the Earth's surface at high spatial resolution (30×30 m^2), and have spectral resolution of 7-10 nm in the 2200-2400 nm band that should also allow useful detection of atmospheric methane. We simulate scenes viewed by EnMAP (10 nm spectral resolution, 180 signal-to-noise ratio) using the EnMAP End-to-End Simulation Tool with superimposed methane plumes generated by large-eddy simulations. We retrieve atmospheric methane and surface reflectivity for these scenes using the IMAP-DOAS optimal estimation algorithm. We find an EnMAP precision of 3-7% for atmospheric methane depending on surface type. This allows effective single-pass detection of methane point sources as small as 100 kg h^{-1} depending on surface brightness, surface homogeneity, and wind speed. Successful retrievals over very heterogeneous surfaces such as an urban mosaic require finer spectral resolution. We tested the EnMAP capability with actual plume observations over oil/gas fields in California from the airborne AVIRIS-NG sensor (3×3 m^2 pixel resolution, 5 nm spectral resolution, SNR 200-400), by spectrally and spatially downsampling the AVIRIS-NG data to match EnMAP instrument specifications. Results confirm that EnMAP can successfully detect point sources of ~100 kg h^{-1} over bright surfaces. Source rates inferred with a generic Integrated Mass Enhancement (IME) algorithm were lower for EnMAP than for AVIRIS-NG. Better agreement may be achieved

31   with a more customized IME algorithm. Our results suggest that imaging spectrometers in space could play an important

32   role in the future for quantifying methane emissions from point sources worldwide.

33

34   **1 Introduction**

35   Methane is a powerful greenhouse gas, but the quantification of sources is highly uncertain. Better quantification

36   is critical for developing strategies to reduce atmospheric methane levels. Anthropogenic emissions originate from a very

37   large number of point sources (coal mine vents, oil/gas facilities, confined livestock operations, landfills, wastewater

38   treatment plants) that are individually small, spatially clustered, temporally variable, and difficult to quantify (Allen et

39   al., 2013; Frankenberg et al., 2016). Here we investigate the potential of new-generation satellite instruments designed

40   to map the Earth's surface at high spatial resolution (imaging spectrometers) to also detect individual methane plumes in

41   the shortwave infrared (SWIR) and from there to quantify the corresponding methane point sources.

42   There has been considerable interest in using SWIR satellite observations of atmospheric methane columns by

43   solar backscatter to detect methane sources and test emission inventories (Jacob et al., 2016). These observations are

44   traditionally made by atmospheric sensors with high spectral resolution (<1 nm) to capture the fine structure of methane

45   rovibrational absorption features (Table 1). The requirement of high spectral resolution has generally forced a coarse

46   pixel resolution (>1 km) to achieve satisfactory signal-to-noise ratios (SNR), but this limits the ability to identify, locate,

47   and quantify individual point sources. Inverse analyses of observations from the SCIAMACHY instrument with 60 km

48   pixel resolution, and from the GOSAT instrument with sparse sampling at 10 km pixel resolution, have quantified

49   emissions over regional scales (Bergamaschi et al., 2009; Kort et al., 2014; Turner et al., 2015). The recently launched

50   TROPOMI instrument with global daily coverage at 7 km nadir pixel resolution (Hu et al., 2018) will refine the regional

51   characterization but still cannot resolve point sources (Sheng et al., 2018). Planned instruments with ~1 km pixel

52   resolution (MethaneSat, CEOS, 2018; Geo-FTS, Xi et al., 2016) should be able to detect large point sources after

53   inversion of several days of observations (Cusworth et al., 2018; Turner et al., 2018) but would not resolve densely

54   clustered or temporally variable sources.

55   Space-based methane sensors have previously focused on achieving high precision (<1%) and low relative bias

56   (<0.3%) for measurements of the dry air column methane mixing ratio (X_{CH4}), as is appropriate for regional

57   characterization of sources (Buchwitz et al., 2015). However, these requirements can be relaxed if the focus is to observe

58   individual plumes. Precision can be traded for pixel resolution because methane plumes are generally sub-kilometer in

59   scale (Frankenberg et al., 2016), so that plume enhancements are larger when the pixel resolution is finer (Jacob et al.,

2016). Bias may not be an issue if the plume enhancement is referenced to the local background. Two commercial instruments, GHGSat and Bluefield Technologies, have recently been developed to observe individual methane plumes (CEOS, 2018). The GHGSat instrument samples selected 12×12 km^2 scenes with 50×50 m^2 effective pixel resolution (McKeever et al., 2017). A demonstration GHGSat instrument (GHGSat-D) launched in 2016, with an estimated precision of about 13%, has proven able to detect large point sources in excess of 1000 kg h^{-1} (Varon et al., 2018b).

Here we examine the potential of a different class of satellite instruments, imaging spectrometers, to detect and quantify individual methane point sources. These instruments are designed for global land surface measurements, but they may be repurposed for non-optimal methane remote sensing. They have fine pixel resolution (<100 m), with much coarser spectral resolution than atmospheric sensors because surface reflectance spectra are relatively smooth. Some current imagers such as Landsat (Roy et al., 2014) and WorldView-3 (http://worldview3.digitalglobe.com) have observing bands in the SWIR to retrieve soil moisture, mineral composition, and vegetation traits (Cleemput et al., 2018). However, the SWIR spectral resolutions for Landsat (100 nm) and WorldView-3 (40-50 nm) are too coarse to usefully resolve methane absorption features. The Hyperion instrument onboard NASA Earth Observing-1 had 10 nm spectral resolution in the SWIR but a low signal to noise ratio (SNR) of 20 (Folkman et al., 2001). Hyperion was able to detect the massive Aliso Canyon methane blowout (Thompson et al., 2016), but its SNR is too low for detection of smaller point sources.

A new generation of imaging spectrometers set for launch over the next decade (EnMAP, PRISMA, EMIT, and the anticipated SBG and CHIME investigations) will achieve ~10 nm or better spectral resolution in the SWIR with pixel resolution in the range 30-60 m and SNR of 180-400 or beyond (Table 1). Experience with airborne imaging spectrometers of comparable specifications suggests that these satellite instruments should be able to observe methane plumes from moderate to large sources. The Airborne Visible/Infrared Imaging Spectrometer (AVIRIS-C), with a 10 nm spectral resolution and SNR of 70 (Green et al., 1998), was able together with Hyperion to detect the massive Aliso Canyon methane leak in California (Thompson et al., 2016). The next generation AVIRIS instrument (AVIRIS-NG), with a finer spectral resolution of 5 nm and SNR of 200 (Thorpe et al., 2014), was able to detect a range of methane plumes over the Four Corners region of New Mexico including from gas processing facilities, storage tanks, pipeline leaks, well pads, and coal mine venting shafts (Frankenberg et al., 2016). AVIRIS-NG has since been flown over 272000 potential methane emitting point sources in California between 2016 and 2018 (CARB, 2017; Duren et al., 2019).

2 Imaging spectrometer spectra including methane plumes

89   Table 1 presents the next generation of spaceborne imaging spectrometers. These include the Italian Space

90   Agency's PRecursore IperSpettrale della Missione Applicativa (PRISMA; Loizzo et al., 2018), launched March 2019;

91   the German Space Agency's Environmental Mapping and Analysis Program (EnMAP; Guanter et al., 2015), scheduled

92   for launch in 2020; NASA's Earth Surface Mineral Dust Source Investigation (EMIT; Green et al., 2018), scheduled for

93   launch to the International Space Station in 2022; as well as NASA's Surface Biology and Geology (SBG; Hochberg et

94   al., 2015) and the European Space Agency's Copernicus Hyperspectral Imaging Mission For The Environment (CHIME;

95   Nieke and Rast, 2018), both of which target launch readiness in the mid-2020s. We will focus our baseline analysis on

96   EnMAP, for which detailed documentation is available (Guanter et al., 2015), and examine other instruments through

97   sensitivity analyses. EnMAP is a push-broom style instrument with 10 nm resolution in the SWIR and an expected 180

98   SNR at 2300 nm. PRISMA has very similar instrument specifications as EnMAP (Loizzo et al., 2018). The EMIT

99   instrument is slated to have a 7-10 nm spectral resolution and 60 m pixel resolution (Green et al., 2018). Other

100   investigations, such as SBG, are called for in the NASA Earth Science and Applications Decadal Survey (National

101   Academies, 2018). The Airbone Methane Plume Spectrometer (AMPS) instrument concept would be tailored specifically

102   for methane detection and have 1 nm SWIR spectral resolution with 30 m pixel resolution (Thorpe et al., 2016).

103   Figure 1 shows simulated transmission spectra in the weak (~1650 nm) and strong (~2300 nm) SWIR methane

104   absorption bands at the spectral resolutions of TROPOMI (0.25 nm full width at half maximum (FWHM)), AVIRIS-NG

105   (5 nm), and EnMAP (10 nm). EnMAP spectra are sampled following the precise wavelength positions given in Guanter

106   et al. (2015). The 1650 nm methane band has the advantage of being near a CO_2 band, so that joint retrievals of methane

107   and CO_2 can be combined with independent knowledge of the CO_2 column mixing ratio to remove joint errors in surface

108   reflectivity and atmospheric scattering (the so-called "CO_2 proxy" method; Frankenberg et al. 2005a). However, the 1650

109   nm band is much weaker than the 2300 nm band and only the 2ν Q-branch can be detected at the EnMAP spectral

110   resolution. Sampling the transmission spectra at the EnMAP spectral resolution yields only 8 data points in the 1650 nm

111   band as compared to 25 in the 2300 nm band. The 2300 nm band also exhibits more resolved structure. Our early attempts

112   to use the CO_2 proxy method in the 1650 nm band with EnMAP synthetic spectra were unsuccessful. In what follows we

113   focus on the 2300 nm band as sampled in the useful 2210 - 2410 nm range.

114   We examined the sensitivity of EnMAP to atmospheric methane by generating synthetic top of atmosphere

115   (TOA) EnMAP scenes with added methane plumes over a variety of surface types. We used for this purpose the EnMAP

116   End-to-End Simulation Tool (EeteS; Segl, 2012), developed to generate EnMAP TOA solar backscattered spectra with

117   expected instrument error included. EeteS takes surface information from another imaging instrument (e.g., SPOT-5),

118 and passes the image through spatial, atmospheric, spectral, and radiometric modules to generate EnMAP spectra. The

119 atmospheric module is based on the MODTRAN5 radiative transfer code (Berk et al., 2006). It assumes a horizontally

120 invariant 1800 ppb X_{CH4} and here we add methane plumes simulated with the Weather and Research Forecasting Model

121 Large Eddy Simulation (WRF-LES) at 30×30 m^2 resolution (Varon et al., 2018a).

122 Figure 2 shows a simulated red-blue-green (RGB) EeteS image over Berlin. We consider four scenes within this

123 domain to add WRF-LES methane plumes and perform subsequent retrievals. The scenes are labelled as Grass, Dark

124 (water), Bright, and Urban. They have mean SWIR surface reflectances of 0.09, 0.02, 0.30, and 0.13, respectively. The

125 urban scene is highly heterogeneous. The WRF-LES simulation is conducted with 30×30 m^2 resolution (the EnMAP

126 pixel resolution), 100 W m^{-2} sensible heat flux (moderately unstable meteorological conditions), and a mean wind speed

127 of 3.5 m s^{-1}. We generate an ensemble of 15 instantaneous plumes by sampling the WRF-LES simulation at five time

128 slices and for three source rates of 100, 500, and 900 kg h^{-1}. This range is typical of large (but not unusually large)

129 individual point sources (Jacob et al., 2016).

130 We compute the optical depth of the methane plume $\tau(\lambda)$ at wavelength λ by multiplying HITRAN absorption

131 cross sections (σ_H; Kochanov et al., 2016) by the methane volume mixing ratio enhancement (ΔVMR) and vertical

132 column density of dry air (VCD) in the 72-layered atmosphere of the MERRA-2 meteorological reanalysis (Gelaro et al.,

133 2017):

$$\tau(\lambda) = \sum_{i=1}^{72} \Delta VMR_i \, VCD_i \, \sigma_{H,i}(\lambda). \quad (1)$$

135

136 Following Beer's law, the plume transmission $T(\lambda)$ is the negative exponential of $\tau(\lambda)$ weighted by the geometric airmass

137 factor A (AMF) for the backscattered solar radiation:

138

$$T(\lambda) = \exp\{-A\tau(\lambda)\}. \quad (2)$$

140

141 Each pixel's EeteS radiance spectrum is multiplied by this additional plume transmission. We do not add noise or aerosol

142 effects to the plume transmission spectra because the EeteS scene already accounts for those in the computation of back-

143 scattered radiances, so that multiplying by the additional plume transmission already factors in the corresponding noise.

144 Figure 3 shows an example WRF-LES plume (500 kg h^{-1} source rate) superimposed over the Grass and Urban scenes.

145   We extended our analysis to other new-generation imaging spectrometers of Table 1 by adapting the EnMAP

146   scenes to different spectral resolutions and SNRs. For this purpose, we interpolated EeteS surface radiance spectra to the

147   desired spectral resolution assuming no instrument noise. We then multiplied these radiance spectra by the transmission

148   spectra from the U.S Standard Atmosphere (Kneizys et al., 1996) with WRF-LES methane plumes added. The SNR

149   values in Table 1 are for a specific reference solar zenith angle (30°) and reflectivity (0.3), but the EeteS radiometric

150   module produces different noise estimates over different surfaces. Here we took the ratios of SNR values relative to

151   EnMAP from Table 1 and applied these ratios to the EeteS noise fields.

152   To test our EnMAP retrievals with actual observations, we also downsampled AVIRIS-NG images taken from

153   aircraft over California (CARB, 2017) to match EnMAP spatial resolution, and further convolved these spectra with the

154   appropriate Gaussian filter to match EnMAP spectral resolution and wavelength positions (Guanter et al., 2015). AVIRIS-

155   NG flew at 3-4 km above the ground, so we simulated additional extinction at higher altitudes based on the U.S Standard

156   Atmosphere. We compared the retrieved methane from AVIRIS-NG and the synthetic EnMAP to determine the ability

157   of EnMAP to detect and quantify the methane point sources identified by AVIRIS-NG.

158

159   **3 Methane retrieval**

160   We retrieved methane from the synthetic imaging spectrometer spectra by adapting the Iterative Maximum A

161   Posteriori - Differential Optical Absorption Spectroscopy (IMAP-DOAS) algorithm developed for AVIRIS (Frankenberg

162   et al., 2005b; Thorpe et al., 2017; Ayasse et al., 2018). DOAS retrievals isolate higher frequency features resulting from

163   gas absorption from lower frequency features that include surface reflectance as well as Rayleigh and Mie scattering

164   (Bovensmann et al., 2011). A polynomial term accounts for the low frequency features (Thorpe et al., 2017).

165

166   *3.1 State vector*

167   In addition to methane (CH_4), the retrieval must account for variable absorption by water vapor (H_2O) and

168   nitrous oxide (N_2O) over the 2210-2400 nm spectral region. We parameterize low frequency spectroscopic features as a

169   sum of Legendre polynomials of order $k = [0, K]$ with coefficients a_k. The state vector (**x**) optimized through the retrieval

170   is composed of the following elements:

171    $$\mathbf{x} = (s_{CH4}, s_{H2O}, s_{N2O}, a_0, ..., a_K)$$

172   where s is a scaling factor applied to the column mixing ratio of each gas from the U.S Standard Atmosphere. We also

173   correct for uncertainty in the instrument's wavelength calibration with a spectral shift parameter, which has been shown

174 in previous studies to reduce wavelength position uncertainty (Thorpe et al., 2017; Frankenberg et al., 2005). EnMAP

175 has strict requirements of 1 nm spectral calibration accuracy and 0.5 nm spectral stability in the SWIR. Pre-flight

176 calibration campaigns as well as onboard calibration means will be used to ensure the compliance with those requirements

177 (Guanter et al., 2015). Additional uncaptured uncertainty in spectral shift may worsen retrieved X_{CH4}. However, given

178 the strong absorption features across the strong 2300 nm CH_4 band, we expect this effect to be small compared other low

179 frequency features, and do not explore this effect further. We do not include aerosols in the retrieval as they play little

180 role at the relevant spatial and spectral resolution (Ayasse et al., 2018). Methane point sources generally do not co-emit

181 aerosols.

182

183 *3.2 Optimal estimation*

184 To retrieve the state vector from the EeteS TOA radiances, we use a forward model similar to previous IMAP-

185 DOAS algorithms (Thorpe et al., 2017, Ayasse et al., 2018), with a modification to the polynomial term for surface

186 reflectance:

187
$$F^h(\mathbf{x}) = I_0(\lambda) \exp \left(-A \sum_{n=1}^{3} s_n \sum_{l=1}^{72} \tau_{n,l} \right) \sum_{k=0}^{K} a_k P_k(\lambda) \quad (3)$$

188 Here F^h is the high-resolution backscattered TOA radiance at wavelength λ, I_0 is the incident TOA solar intensity, $\tau_{n,l}$ is

189 the default optical depth from the U.S Standard Atmosphere for trace gas element $n = [1,3]$ of the state vector at vertical

190 level $l = [1,72]$, s_n is the scaling factor to that default optical depth optimized in the retrieval, P_k is the kth Legendre

191 polynomial, and the a_k are coefficients optimized in the retrieval. The optical depth $\tau_{n,l}$ is computed in the same fashion

192 as Equation 1, using information from the MERRA-2 reanalysis and HITRAN absorption cross sections. For satellite

193 retrievals, the AMF is a scalar describing the optical path through the atmosphere. In Section 4.3, we apply the IMAP-

194 DOAS algorithm to airborne AVIRIS-NG scenes and use a vector-valued AMF that depends on the height of the aircraft.

195 Previous IMAP-DOAS algorithms used a simple polynomial approximation for the surface reflectance, but here

196 we use Legendre polynomials to exploit their orthogonality. Orthogonal polynomials can potentially constrain surface

197 reflectance with fewer terms, leading to better conditioning of the inverse solution. We find that $K = 4$ provides sufficient

198 spectral resolution whereas previous applications using simple polynomials required $K = 6$ (Ayasse et al., 2018).

199 We compute the TOA backscattered radiances $F^h(\mathbf{x})$ over the 2210-2410 nm spectral range at 0.02 nm

200 resolution, and assemble these in a vector $\mathbf{F^h(x)}$ representing the high-resolution spectrum as simulated by the forward

201 model for a given $\mathbf{x}$. We convolve this spectrum with the instrument FWHM and then sample at the known wavelength

positions. For example, for EnMAP, we convolve $\mathbf{F}^h(\mathbf{x})$ with a 10 nm FWHM and sample the resulting spectra at EnMAP's 10 nm intervals to get the low-resolution $\mathbf{F}(\mathbf{x})$. Since the convolution operator is not linear (Frankenberg et al., 2005), we also explored performing separate convolutions on the high resolution transmission and polynomial terms in Equation 3, and then multiplying them together to get $\mathbf{F}(\mathbf{x})$. We found little difference in the results between methods.

Observed backscattered TOA radiances ($\mathbf{y}$) can be represented as

$$\mathbf{y} = \mathbf{F}(\mathbf{x}) + \boldsymbol{\epsilon} \quad (4)$$

where the observational error $\boldsymbol{\epsilon}$ is the sum of instrument and forward model errors. As is commonly done for satellite retrievals, we assume that the forward model error is small compared to the instrument error characterized by the SNR. The forward model is non-linear so that the solution must be obtained iteratively. A Jacobian matrix is calculated for each iteration i of the state vector

$$\mathbf{K}_i = \left.\frac{\partial \mathbf{F}}{\partial \mathbf{x}}\right|_{\mathbf{x}=\mathbf{x}_i} \quad (5)$$

and we employ a Gauss-Newton iteration to solve iteratively for the optimal state vector (Rodgers, 2000):

$$\mathbf{x}_{i+1} = \mathbf{x_A} + (\mathbf{K}_i^T \mathbf{S_O^{-1}} \mathbf{K}_i + \mathbf{S_A^{-1}})^{-1} \mathbf{K}_i^T \mathbf{S_O^{-1}}[y - \mathbf{F}(\mathbf{x}_i) + \mathbf{K}_i(\mathbf{x}_i - \mathbf{x_A})] \quad (6)$$

Here $\mathbf{S_O} = [\boldsymbol{\epsilon\epsilon}^T]$ is the observation error covariance matrix defined by the instrument SNR, $\mathbf{x_A}$ is the prior estimate of the state vector, and $\mathbf{S_A}$ is the prior error covariance matrix. We set a weak prior error variance for methane, (unitless)

$$\hat{\mathbf{S}} = \left(\mathbf{K}_i^{\mathbf{T}} \mathbf{S_O^{-1}} \mathbf{K}_i + \mathbf{S_A^{-1}}\right)^{-1} \quad (7)$$

$\hat{\mathbf{S}}$ gives information on the error correlation between retrieved methane and surface reflectivity, which is a major concern for methane retrievals (Butz et al., 2012).

3.3 Inferring point source rates from methane plume observations

The plume observations can be related to the corresponding source rates by computing the integrated mass enhancements (IME) within the plume mask (Frankenberg et al., 2016; Varon et al., 2018a). Following Varon et al. (2018a), we define the plume for the retrieved scenes with a plume mask that applies median and Gaussian filters to pixels above the 80th percentile of X_{CH4} within the scene. These filters help to remove spurious signals surrounding a plume and determine the spatial extent of the plume, which is needed for subsequent calculations. The IME is calculated as:

$$\text{IME} = \sum_{i=1}^{N} \Delta\Omega_i \Lambda_i \quad (8)$$

230   where $\Delta\Omega_i$ is the plume mass enhancement in pixel i relative to background (kg m^{-2}), Λ_i is the corresponding area of the

231   pixel, and the summation is over the N pixels within the plume mask. Here, we define the background as the median X_{CH4}

232   within the scene. The point source rate Q is then inferred from the IME as (Varon et al., 2018a)

233
$$Q = \frac{U_{eff}}{L} \text{ IME} \quad (9)$$

234   where $L = \sqrt{\sum_{i=1}^{N} \Lambda_i}$ is a characteristic plume size and U_{eff} is an effective wind speed describing the rate of turbulent

235   dissipation of the plume (L/U_{eff} is the lifetime of the plume against turbulent dissipation to below the detection limit).

236   Varon et al. (2018a) relate U_{eff} to the 10-m wind speed (U_{10}) by fitting to WRF-LES simulations. Here we use their

237   relationship derived for the GHGSat instrument with 50 m pixel resolution and 5% precision:

238
$$U_{eff} = 1.1 \log U_{10} + 0.6 \quad (10)$$

239   where U_{eff} and U_{10} are in units of [m s^{-1}]. The U_{eff}-U_{10} relationship should depend on the instrument pixel resolution and

240   precision, and on the plume masking procedure, which would require customized WRF-LES simulations and fitting.

241   Here we simply apply equation (10) to the AVIRIS-NG and EnMAP plumes without further modification. In Section 4.3,

242   we do not a priori know the wind speed, and obtain U_{10} from the HRRR-Reanalysis at 3-km hourly resolution

243   (https://rapidrefresh.noaa.gov/).

244

245

246   **4. Results and Discussion**

247   *4.1 EnMAP plume retrievals over different surfaces*

248   Figure 3 shows examples of the IMAP-DOAS retrievals of 500 kg h^{-1} and 900 kg h^{-1} WRF-LES plumes over

249   the Grass and Urban scenes. The 500 kg h^{-1} plume is clearly defined in the Grass scene near the emission source. It is

250   also detectable in the Urban scene but obscured by retrieval artifacts, as some of the variability in surface reflectivity is

251   erroneously retrieved as methane variability. The 900 kg h^{-1} plume is better captured over both surfaces, though major

252   retrieval artifacts remain in the Urban scene.

253   Varon et al. (2018a) previously estimated the theoretical ability of a satellite instrument to quantify source rates

254   from point sources as a function of instrument precision, assuming a uniform surface reflectance. They concluded that

255   an instrument with 1-5% precision for X_{CH4} would be able to quantify point sources with an error of 70-170 kg h^{-1}. Here

256   we characterize the EnMAP instrument precision as the relative residual standard deviation (RRSD) between the true

257   and retrieved column methane concentrations for individual 30×30 m^2 pixels in the scenes of Figure 2 including the

258   WRF-LES plumes. Figure 4 summarizes the results for the four scenes of Figure 2. We find precisions of $3.5 \pm 0.07\%$

259   for Grass, $7.2 \pm 0.1\%$ for Urban, and $2.6 \pm 0.08\%$ for Bright scenes. The standard deviations refer to the RRSDs computed

260   for the 15 different realizations of the WRF-LES plumes and for the 3 source rates of 100, 500, and 900 kg h^{-1}. The Dark

261   scene was consistently unsuccessful, with error of at least 100% for each realization, and we do not discuss it further.

262   The Bright scene performs the best because of the large backscattered photon flux. The Urban scene performs worse than

263   the Grass scene, even though its average SWIR surface reflectance is larger, due to the larger variability in reflectance

264   over the scene including dark pixels.

265   We examined the ability of the retrievals to quantify methane point source rates on the basis of the detected

266   plumes, by applying the IME algorithm of Section 3.3 to the same ensemble of 5 WRF-LES plume realizations for each

267   of the three different surfaces and for true source rates 100, 500, and 900 kg h^{-1}. Results are summarized in Table 2. We

268   find that it is possible to quantify source rates as low as 100 kg h^{-1} for the Bright scene, and as low as 500 kg h^{-1} for the

269   Grass scene, though the true source rates are underestimated by up to a factor of 2. There could be several factors behind

270   this underestimate including (1) error correlation with surface reflectivity in the EnMAP retrieval that would cause some

271   loss of the plume, and (2) use of the Varon et al. (2018a) U_{eff}-U_{10} relationship in equation (10) without customization for

272   the EnMAP conditions. As pointed out by Varon et al. (2018a), the U_{eff}-U_{10} relationship should be customized to the

273   plume mask definition and to the instrument pixel resolution and precision. This would require an ensemble of WRF-

274   LES simulations specific to the EnMAP conditions and to the plume mask used here. The inability to quantify the 100

275   kg h^{-1} plume over the Grass scene is properly diagnosed in our retrieval by the failure of the plume mask to detect a

276   plume. However, the surface artifacts in the Urban scene lead to spurious retrievals of source rates as the surface features

277   are mistakenly attributed to plumes. This is due to the error correlation between X_{CH4} and surface reflectivity (explained

278   in greater detail in Section 4.2) and can be diagnosed by inspection of the off-diagonal terms of $\hat{\mathbf{S}}$ (Equation 7).

279

280   *4.2 Sensitivity to instrument spectral resolution and SNR*

281   We examine the potential of future imaging spectrometers with improved spectral resolution and SNR relative

282   to EnMAP (Table 1) to achieve improved retrievals of point sources. Figure 5 shows the change in the methane retrieval

283   precision as we vary the spectral resolution from 10 to 1 nm and the mean scene-wide SNR from 100 to 500.

284   Specifications of the instruments in Table 1 are identified on the plot. Precision improves as spectral resolution and SNR

285   increase, as expected. The dependencies are not linear, and the contours are concave, meaning that precision is more

286   effectively improved by increasing spectral resolution by a certain factor than by increasing SNR by the same factor.

287 Increasing the spectral resolution improves precision through multiple independent factors: by increasing the number of

288 independent measurements across the useful spectral window; by increasing the effective squared depth of the sharpest

289 methane absorptions, for improved spectral contrast relative to the continuum; and by better resolution of the unique

290 methane absorption shape, which improves discrimination against potential surface confusers.

291   We saw in Figure 3 that the inability to decouple surface and methane features at low spectral resolution was a

292 major source of error over inhomogeneous surfaces such as the Urban scene. This is manifested in the retrieval by an

293 error correlation between state vector elements s_{CH4} (scaling factor for methane column mixing ratios) and a_k (coefficients

294 for the surface reflectivity described by Legendre polynomials). This error correlation is described by the posterior error

295 covariance matrix $\hat{\mathbf{S}}$ obtained as part of the retrieval (Equation 7). The bivariate probability density between retrieved

296 X_{CH4} and the mean SWIR surface reflectivity can be obtained by summing the error covariances of the Legendre

297 polynomial terms. We find in this manner that the error correlation between X_{CH4} and the mean SWIR surface reflectivity

298 for the Urban scene decreases between EnMAP ($r = -0.33$) and AMPS ($r = -0.19$). This is driven by the increase in

299 spectral resolution from 10 nm to 1 nm. We further find that simply increasing the SNR to 300 (as recommended for

300 SBG) while keeping spectral resolution constant does not improve the error correlation.

301   A related benefit of decoupling X_{CH4} from the surface reflectance in the retrieval is to improve the capability for

302 plume pattern recognition, which is necessary to convert observed plume methane enhancements into source rates. Figure

303 6 illustrates this for the Grass and Urban scenes of Figure 3 including the plume from the 500 kg h^{-1} point source.

304 Retrievals are performed with the specifications of the EnMAP instrument (10 nm spectral resolution, SNR 180), SBG

305 (10 nm, 300), and AMPS (1 nm, 400). For the Grass scene we find that all three instruments can discern the plume pattern

306 near the emission source and separate it from surface features. SBG and AMPS capture larger plume domains because

307 of their higher precisions (Figure 5), which would improve the inference of the source rates. For the Urban scene, EnMAP

308 plume detection is swamped by surface artifacts. Simply increasing the SNR as in the SBG instrument does not improve

309 the situation. Increasing the spectral resolution to 1 nm as in the AMPS instrument enables detection of the plume though

310 quantification is still compromised by surface artifacts.

311

312 *4.3 Evaluation with AVIRIS-NG observations*

313   To test the EnMAP retrieval capability with actual observations, we downsampled AVIRIS-NG airborne spectra

314 taken over California methane emitting facilities (CARB, 2017). We chose three scenes observed by AVIRIS-NG on

315 different days over oil and gas facilities. Figure 7 shows the RGB images, the AVIRIS-NG plume retrievals performed

316   by applying the method of Section 3 with a variable AMF, and the downsampled EnMAP retrievals. Plume masks were

317   applied as described in Section 3.3 and shown in Figure 6. At the altitudes used for the California survey, AVIRIS-NG

318   has 3×3 m^2 pixel resolution and hence features much sharper methane enhancements than EnMAP (note the different

319   scales for the middle and right panels). Nevertheless, we see from Figure 7 that EnMAP is able to detect the same plumes

320   as AVIRIS-NG (two plumes in the bottom panels). This is facilitated by the brightness of the surfaces. The surface

321   reflectivities retrieved simultaneously with the methane enhancements in our IMAP-DOAS algorithm are 0.39-0.49,

322   brighter than the Bright EeteS scene in Section 4.1.

323   Figure 7 shows the source rates inferred from the AVIRIS-NG and EnMAP retrievals for each point source. The

324   AVIRIS-NG source rates are a factor of 1.2-3.0 greater (average 1.9) than the EnMAP source rates. The EnMAP

325   underestimate is consistent with the results in Table 2 and may reflect the same sources of bias, in part correctable through

326   an improved U_{10}-U_{eff} relationship. The results confirm that EnMAP should be able to detect plumes and estimate source

327   rates down to ~100 kg h^{-1} when the scene is sufficiently bright.

328

329   **5 Conclusions**

330   We examined the potential of next-generation spaceborne imaging spectrometers (EnMAP, PRISMA, EMIT,

331   SBG, CHIME) for observing atmospheric methane plumes from point sources and inferring the corresponding source

332   rates. These instruments have launch dates of 2019-2025 and focus on observing the Earth surface with fine pixel

333   resolution (30×30 m^2), including observing channels at 2200-2400 nm with 7-10 nm spectral resolution that could also

334   be used to retrieve methane plumes. This would achieve much finer spatial resolution than the standard satellite

335   instruments designed to measure atmospheric methane and would provide a unique resource for global mapping of

336   individual methane point sources.

337   We focused our baseline analysis on EnMAP (spectral resolution 10 nm, SNR 180, 2020 launch date) as its

338   specifications are well documented (Guanter et al, 2015). We created synthetic spectra using the EnMAP End-to-End

339   Simulation Tool (EeteS) to simulate various surface scenes (Grass, Urban, Bright) with instrument errors and with

340   superimposed methane plumes generated by a WRF Large Eddy Simulation (LES). We then retrieved these scenes for

341   atmospheric methane together with surface reflectivities (fitted with Legendre polynomials) using the Iterative Maximum

342   A Posteriori - Differential Optical Absorption Spectroscopy (IMAP-DOAS) approach. The resulting precisions for

343   methane are 3.5% for the Grass scene, 7.2% for Urban, and 2.6% for Bright. A 500 kg h^{-1} methane plume (typical of very

344 large point sources) is readily detected over the relatively homogeneous Grass surface. The highly heterogeneous Urban

345 surface is much more challenging because of retrieval artifacts.

346   The limitation of EnMAP in detecting methane plumes over heterogeneous surfaces is caused by error

347 correlation between methane and surface reflectivity in the retrieval. We examined how precision and error correlation

348 could be improved by increasing spectral resolution and SNR. We find that increasing spectral resolution reduces the

349 error correlation more efficiently than increasing SNR by enabling separation of fine spectral structure (methane) from

350 coarse spectral structure (surface). The Atmospheric Methane Plume Spectrometer (AMPS) instrument concept, which

351 bridges the gap between imaging spectrometers and spaceborne methane sensors (1 nm spectral resolution, SNR 400),

352 can greatly decrease surface artifacts and detect a 500 kg h^{-1} plume even over the heterogeneous Urban surface.

353 Alternative retrieval parameterizations might also improve separation of methane and surface reflectivity features.

354 (Thompson et al., 2018; Ong et al., 2019).

355   We tested the EnMAP capability with actual observations by downsampling AVIRIS-NG images taken from

356 aircraft (3×3 m^2 pixels, 5 nm spectral resolution, SNR 200) over California methane emitting facilities (CARB, 2017).

357 We showed that these EnMAP-like images are able to detect actual plumes of magnitude ~100 kg h^{-1} over relatively

358 bright surfaces. Source rates inferred from the plumes with a generic Integrated Mass Enhancement (IME) method are a

359 factor of 1.2 to 3 lower for EnMAP than for AVIRIS-NG, which could be due in part to unaccounted dependence of the

360 IME method on instrument pixel size and precision. This should be improved in further work by customizing the IME

361 method to the EnMAP specifications.

362   In summary, our analysis shows that future spaceborne imaging spectrometers designed to map land surfaces in

363 the SWIR also have potential for detecting methane plumes from point sources and quantifying source rates. The

364 detection capability of 100-500 kg h^{-1} over relatively bright and homogeneous land surfaces would allow accounting for

365 a wide range of point sources. The fine spatial resolution of these instruments should make them a unique resource to

366 contribute to tiered observing systems for greenhouse gases (Duren and Miller, 2012).

367

368 **Data Availability**. Example EeteS scenes are available at http://www.enmap.org/node/21.html. WRF-LES simulations

369 are available upon request. HITRAN absorption cross-sections are available at https://hitran.org/hapi/. AVIRIS-NG raw

370 radiances are available at https://avirisng.jpl.nasa.gov/alt_locator/. MERRA-2 reanalysis is available at

371 https://gmao.gsfc.nasa.gov/reanalysis/MERRA-2/.

372

373   **Author contributions**. DHC performed the main analysis, created figures, and wrote the manuscript. DJJ and CRR

374   helped develop the analysis, scientific interpretation, and manuscript. DJV performed WRF-LES simulations. CCM, XL,

375   and KC provided guidance on radiative transfer simulations. AKT and CF helped with the development of the IMAP-

376   DOAS retrieval. AKT, RMD, CEM, and DRT provided guidance on the AVIRIS-NG instrument, campaigns, and

377   retrieval. LG provided EeteS simulations. All authors provided comments to the manuscript.

378

379   **Competing interests**. The authors declare they have no conflict of interest.

380

381   **Acknowledgments**. This work was supported in part by the ExxonMobil Research and Engineering Company and

382   NASA's Carbon Monitoring System (CMS) Prototype Methane Monitoring System for California. Data from the

383   California Methane Survey was supported by NASA's Earth Science Division, the California Air Resources Board under

384   ARB-NASA Agreement 15RD028 Space Act Agreement 82-19863 and the California Energy Commission under CEC-

385   500-15-004. Portions of this work was undertaken at the Jet Propulsion Laboratory, California Institute of Technology,

386   under contract with NASA

References

Allen, D. T., Torres, V. M., Thomas, J., Sullivan, D. W., Harrison, M., Hendler, A., Herndon, S. C., Kolb, C. E., Fraser, M. P., Hill, A. D., Lamb, B. K., Miskimins, J., Sawyer, R. F., and Seinfeld, J. H.: Measurements of methane emissions at natural gas production sites in the United States, Proceedings of the National Academy of Sciences, 110, 17 768–17 773, doi:10.1073/ pnas.1304880110, URL https://www.pnas.org/content/110/44/17768, 2013.

Ayasse, A. K., Thorpe, A. K., Roberts, D. A., Funk, C. C., Dennison, P. E., Frankenberg, C., Steffke, A., and Aubrey, A. D.: Evaluating the effects of surface properties on methane retrievals using a synthetic airborne visible/infrared imaging spectrometer next generation (AVIRIS-NG) image, Remote Sensing of Environment, 215, 386 – 397, doi:https://doi. org/10.1016/j.rse.2018.06.018, URL http://www.sciencedirect.com/science/article/ pii/S0034425718302967, 2018.

Bergamaschi, P., Frankenberg, C., Meirink, J. F., Krol, M., Villani, M. G., Houweling, S., Dentener, F., Dlugokencky, E. J., Miller, J. B., Gatti, L. V., Engel, A., and Levin, I.: Inverse modeling of global and regional CH4 emissions using SCIAMACHY satellite retrievals, Journal of Geophysical Research: Atmospheres, 114, doi:10.1029/2009JD012287, URL https:// agupubs. onlinelibrary.wiley.com/doi/abs/10.1029/2009JD012287, 2009.

Berk, A., Anderson, G. P., Acharya, P. K., Bernstein, L. S., Muratov, L., Lee, J., Fox, M., Adler-Golden, S. M., Chetwynd Jr, J. H., Hoke, M. L., et al.: MODTRAN5: 2006 update, in: Algorithms and Technologies for Multispectral, Hyperspectral, and Ultraspectral Imagery XII, vol. 6233, p. 62331F, International Society for Optics and Photonics, 2006.

Bovensmann, H., Doicu, A., Stammes, P., Van Roozendael, M., Von Savigny, C., de Vries, M. P., Beirle, S., Wagner, T., Chance, K., Buchwitz, M., et al.: From Radiation Fields to Atmospheric Concentrations–Retrieval of Geophysical Parameters, in: SCIAMACHY-Exploring the Changing Earth's Atmosphere, pp. 99–127, Springer, 2011.

Buchwitz, M., Reuter, M., Schneising, O., Boesch, H., Guerlet, S., Dils, B., Aben, I., Armante, R., Bergamaschi, P., Blumenstock, T., Bovensmann, H., Brunner, D., Buchmann, B., Burrows, J., Butz, A., Che´din, A., Chevallier, F., Crevoisier, C., Deutscher, N., Frankenberg, C., Hase, F., Hasekamp, O., Heymann, J., Kaminski, T., Laeng, A., Lichtenberg, G., Mazie`re, M. D., Noe¨l, S., Notholt, J., Orphal, J., Popp, C., Parker, R., Scholze, M., Sussmann, R., Stiller, G., Warneke, T., Zehner, C., Bril, A., Crisp, D., Griffith, D., Kuze, A., O'Dell, C., Oshchepkov, S., Sherlock, V., Suto, H., Wennberg, P., Wunch, D., Yokota, T., and Yoshida, Y.: The Greenhouse Gas Climate Change Initiative (GHG-CCI): Comparison and quality assessment of near-surface-sensitive satellite-derived CO2 and CH4 global data sets, Remote Sensing of Environment, 162, 344 – 362, doi:https://doi.org/10.1016/j.rse.2013.04.024, URL http://www.sciencedirect.com/science/article/pii/S0034425713003520, 2015.

Butz, A., Galli, A., Hasekamp, O., Landgraf, J., Tol, P., and Aben, I.: TROPOMI aboard Sentinel-5 Precursor: Prospective performance of CH4 retrievals for aerosol and cirrus loaded atmospheres, Remote Sensing of Environment, 120, 267 – 276, doi:https://doi.org/10.1016/j.rse.2011.05.030, URL http://www.sciencedirect.com/science/article/pii/S003442571200082X, the Sentinel Missions - New Opportunities for Science, 2012.

CARB: Introduction to the Phase I Report of the California Methane Survey from the Staff of the California Air Resources Board (CARB), Tech. rep., The California Air Resources Board, URL https://ww3.arb.ca.gov/research/methane/ca_ch4_survey_phase1_report_2017. pdf?_ga=2.259065807.470178342.1556320978-319883758.1556320978, 2017.

35

40

CEOS: A Constellation Architecture for Monitoring Carbon Dioxide and Methane from Space, Tech. rep., University of Zurich, Department of Informatics, URL http://ceos.org/document_management/Meetings/Plenary/32/documents/CEOS_ AC-VC_White_Paper_Version_1_20181009.pdf, 2018.

5 Cleemput, E. V., Vanierschot, L., Ferna´ndez-Castilla, B., Honnay, O., and Somers, B.: The functional characterization of grass- and shrubland ecosystems using hyperspectral remote sensing: trends, accuracy and moderating variables, Remote Sensing of Environment, 209, 747 − 763, doi:https://doi.org/10.1016/j.rse.2018.02.030, URL http://www.sciencedirect.com/ science/article/pii/S0034425718300427, 2018.

10 Cusworth, D. H., Jacob, D. J., Sheng, J.-X., Benmergui, J., Turner, A. J., Brandman, J., White, L., and Randles, C. A.: Detecting high-emitting methane sources in oil/gas fields using satellite observations, Atmospheric Chemistry and Physics, 18, 16 885–16 896, doi:10.5194/ acp-18-16885-2018, URL https://www.atmos-chem-phys.net/18/16885/2018/, 2018.

Duren, R. M. and Miller, C. E.: Measuring the carbon emissions of megacities, Nature Climate Change, 2, 560, 2012.

Duren, R. M., Thorpe, A. K., Foster, K. T., Rafiq, T., Hopkins, F. M., Yadav, V., Bue, B., Thompson, D. R., Conley, S.,
15 Colombi, N., Frankenberg, C., McCubbin, I., Eastwood, M. L., Falk, M., Herner, J., Croes, B. E., Green, R. O., and Miller, C. M.: California?s Methane Super-emitters, Nature, 2019.

Folkman, M. A., Pearlman, J., Liao, L. B., and Jarecke, P. J.: EO-1/Hyperion hyperspectral imager design, development, characterization, and calibration, in: Hyperspectral Remote Sensing of the Land and Atmosphere, vol. 4151, pp. 40–52, International Society for Optics and Photonics, 2001.

20 Frankenberg, C., Meirink, J. F., van Weele, M., Platt, U., and Wagner, T.: Assessing Methane Emissions from Global Space-Borne Observations, Science, 308, 1010–1014, doi:10. 1126/science.1106644, URL http://science.sciencemag.org/content/308/5724/1010, 2005.

Frankenberg, C., Platt, U., and Wagner, T.: Iterative maximum a posteriori (IMAP)-DOAS for retrieval of strongly absorbing trace gases: Model studies for CH4 and CO2 retrieval from near infrared spectra of SCIAMACHY onboard ENVISAT,
25 Atmospheric Chemistry and Physics, 5, 9–22, doi:10.5194/acp-5-9-2005, URL https://www.atmos-chem-phys.net/5/9/2005/, 2005b.

Frankenberg, C., Meirink, J., Bergamaschi, P., Goede, A., Heimann, M., Ko¨rner, S., Platt, U., van Weele, M., and Wagner, T.: Satellite chartography of atmospheric methane from SCIAMACHY on board ENVISAT: Analysis of the years 2003
30 and 2004, Journal of Geophysical Research: Atmospheres, 111, 2006.

Frankenberg, C., Thorpe, A. K., Thompson, D. R., Hulley, G., Kort, E. A., Vance, N., Borchardt, J., Krings, T., Gerilowski, K., Sweeney, C., Conley, S., Bue, B. D., Aubrey, A. D., Hook, S., and Green, R. O.: Airborne methane remote measurements reveal heavy-tail flux distribution in Four Corners region, Proceedings of the National Academy of
35 Sciences, 113, 9734–9739, doi:10.1073/pnas.1605617113, URL https://www.pnas.org/content/113/35/9734, 2016.

Gelaro, R., McCarty, W., Sua´rez, M. J., Todling, R., Molod, A., Takacs, L., Randles, C. A., Darmenov, A., Bosilovich, M. G., Reichle, R., Wargan, K., Coy, L., Cullather, R., Draper, C., Akella, S., Buchard, V., Conaty, A., da Silva, A. M., Gu, W., Kim, G.-K., Koster, R., Lucchesi, R., Merkova, D., Nielsen, J. E., Partyka, G., Pawson, S., Putman, W., Rienecker, M., Schubert, S. D., Sienkiewicz, M., and Zhao, B.: The Modern-Era Retrospective Analysis for Research and
40 Applications, Version 2 (MERRA-2), Journal of Climate, 30, 5419–5454, doi:10.1175/ JCLI-D-16-0758.1, URL https://doi.org/10.1175/JCLI-D-16-0758.1, 2017.

Green, R., Mahowald, N., Clark, R., Ehlmann, B., Ginoux, P., Kalashnikova, O., Miller, R., Okin, G., Painter, T., Pe´rez Garc´ıa-Pando, C., et al.: NASA's Earth Surface Mineral Dust Source Investigation, in: AGU Fall Meeting Abstracts, 2018.

5   Green, R. O., Eastwood, M. L., Sarture, C. M., Chrien, T. G., Aronsson, M., Chippendale, B. J., Faust, J. A., Pavri, B. E., Chovit, C. J., Solis, M., Olah, M. R., and Williams, O.: Imaging Spectroscopy and the Airborne Visible/Infrared Imaging Spectrometer (AVIRIS), Remote Sensing of Environment, 65, 227 – 248, doi:https://doi.org/10.1016/ S0034-4257(98)00064-9, URL http://www.sciencedirect.com/science/article/pii/ S0034425798000649, 1998.

Guanter, L., Kaufmann, H., Segl, K., Foerster, S., Rogass, C., Chabrillat, S., Kuester, T., Hollstein, A., Rossner, G., Chlebek, C., Straif, C., Fischer, S., Schrader, S., Storch, T., Heiden, U., Mueller, A., Bachmann, M., Mu¨hle, H., Mu¨ller, R.,
10   Habermeyer, M., Ohndorf, A., Hill, J., Buddenbaum, H., Hostert, P., Van der Linden, S., Leita˜o, P. J., Rabe, A., Doerffer, R., Krasemann, H., Xi, H., Mauser, W., Hank, T., Locherer, M., Rast, M., Staenz, K., and Sang, B.: The EnMAP Spaceborne Imaging Spectroscopy Mission for Earth Observation, Remote Sensing, 7, 8830–8857, doi:10.3390/rs70708830, URL http://www.mdpi.com/2072-4292/7/7/8830, 2015.

15   Hochberg, E. J., Roberts, D. A., Dennison, P. E., and Hulley, G. C.: Special issue on the Hyperspectral Infrared Imager (HyspIRI): Emerging science in terrestrial and aquatic ecology, radiation balance and hazards, Remote Sensing of Environment, 167, 1 – 5, doi:https://doi. org/10.1016/j.rse.2015.06.011, URL http://www.sciencedirect.com/science/article/ pii/S0034425715300420, special Issue on the Hyperspectral Infrared Imager (HyspIRI), 2015.

20   Hu, H., Landgraf, J., Detmers, R., Borsdorff, T., Aan de Brugh, J., Aben, I., Butz, A., and Hasekamp, O.: Toward Global Mapping of Methane With TROPOMI: First Results and Intersatellite Comparison to GOSAT, Geophysical Research Letters, 45, 3682–3689, doi:10. 1002/2018GL077259, URL https://agupubs.onlinelibrary.wiley.com/doi/abs/10. 1002/2018GL077259, 2018.

Jacob, D. J., Turner, A. J., Maasakkers, J. D., Sheng, J., Sun, K., Liu, X., Chance, K., Aben, I., McKeever, J., and
25   Frankenberg, C.: Satellite observations of atmospheric methane and their value for quantifying methane emissions, Atmospheric Chemistry and Physics, 16, 14 371–14 396, doi:10.5194/acp-16-14371-2016, URL https://www.atmos-chem-phys. net/16/14371/2016/, 2016.

Kneizys, F., Abreu, L., Anderson, G., Chetwynd, J., Shettle, E., Berk, A., Bernstein, L., Robertson, D., Acharya, P., and
30   Rothman, L.: The MODTRAN 2/3 report and LOWTRAN 7 model, Phillips Laboratory, Hanscom AFB, MA, 1731, 1996.

Kochanov, R., Gordon, I., Rothman, L., Wcisło, P., Hill, C., and Wilzewski, J.: HITRAN Application Programming Interface (HAPI): A comprehensive approach to working with spectroscopic data, Journal of Quantitative Spectroscopy and Radiative Transfer, 177, 15–30, doi:https://doi.org/10.1016/j.jqsrt.2016.03.005, URL http://www.sciencedirect. com/science/article/pii/S0022407315302466, xVIIIth Symposium on High Resolution Molecular Spectroscopy
35   (HighRus-2015), Tomsk, Russia, 2016.

Kort, E. A., Frankenberg, C., Costigan, K. R., Lindenmaier, R., Dubey, M. K., and Wunch, D.: Four corners: The largest US methane anomaly viewed from space, Geophysical Research Letters, 41, 6898–6903, doi:10.1002/2014GL061503, URL https://agupubs.onlinelibrary.wiley. com/doi/abs/10.1002/2014GL061503.

Kuze, A., Suto, H., Shiomi, K., Kawakami, S., Tanaka, M., Ueda, Y., Deguchi, A., Yoshida, J., Yamamoto, Y., Kataoka, F.,
40   et al.: Update on GOSAT TANSO-FTS performance, operations, and data products after more than 6 years in space., Atmospheric Measurement Techniques, 9, 2016.

Loizzo, R., Guarini, R., Longo, F., Scopa, T., Formaro, R., Facchinetti, C., and Varacalli, G.: Prisma: The Italian Hyperspectral Mission, in: IGARSS 2018 - 2018 IEEE International Geoscience and Remote Sensing Symposium, pp. 175–178, doi:10.1109/IGARSS.2018. 8518512, 2018.

McKeever, J., Durak, B., Gains, D., Jervis, D., Varon, D., Germain, S., and Sloan, J.: GHGSat-D: Greenhouse gas plume imaging and quantification from space using a Fabry-Perot imaging spectrometer, Abstract (A33G-2450) presented at 2017 AGU Fall Meeting, New Orleans, LA, 11–15 December, 2017AGUFM, 2017.

National Academies of Sciences, E. and Medicine: Thriving on Our Changing Planet: A Decadal Strategy for Earth Observation from Space, The National Academies Press, Washington, DC, doi:10.17226/24938, URL https://www.nap.edu/catalog/24938/ thriving-on-our-changing-planet-a-decadal-strategy-for-earth, 2018.

Nieke, J. and Rast, M.: Towards the Copernicus Hyperspectral Imaging Mission For The Environment (CHIME), in: IGARSS 2018 - 2018 IEEE International Geoscience and Remote Sensing Symposium, pp. 157–159, doi:10.1109/IGARSS.2018.8518384, 2018.

Rodgers, C. D.: Inverse methods for atmospheric sounding: theory and practice, vol. 2, World scientific, 2000.

Roy, D., Wulder, M., Loveland, T., C.E., W., Allen, R., Anderson, M., Helder, D., Irons, J., Johnson, D., Kennedy, R., Scambos, T., Schaaf, C., Schott, J., Sheng, Y., Vermote, E., Belward, A., Bindschadler, R., Cohen, W., Gao, F., Hipple, J., Hostert, P., Huntington, J., Justice, C., Kilic, A., Kovalskyy, V., Lee, Z., Lymburner, L., Masek, J., McCorkel, J., Shuai, Y., Trezza, R., Vogelmann, J., Wynne, R., and Zhu, Z.: Landsat-8: Science and product vision for terrestrial global change research, Remote Sensing of Environment, 145, 154 – 172, doi:https://doi.org/10.1016/j.rse.2014.02.001, URL http://www.sciencedirect.com/ science/article/pii/S003442571400042X, 2014.

Segl, K., Guanter, L., Rogass, C., Kuester, T., Roessner, S., Kaufmann, H., Sang, B., Mogulsky, V., and Hofer, S.: EeteS— The EnMAP End-to-End Simulation Tool, IEEE Journal of Selected Topics in Applied Earth Observations and Remote Sensing, 5, 522–530, doi:10.1109/JSTARS. 2012.2188994, 2012.

Sheng, J.-X., Jacob, D. J., Maasakkers, J. D., Zhang, Y., and Sulprizio, M. P.: Comparative analysis of low-Earth orbit (TROPOMI) and geostationary (GeoCARB, GEO-CAPE) satellite instruments for constraining methane emissions on fine regional scales: application to the Southeast US, Atmospheric Measurement Techniques, 11, 6379–6388, doi:10.5194/ amt-11-6379-2018, URL https://www.atmos-meas-tech.net/11/6379/2018/, 2018.

Thompson, D. R., Thorpe, A. K., Frankenberg, C., Green, R. O., Duren, R., Guanter, L., Hollstein, A., Middleton, E., Ong, L., and Ungar, S.: Space-based remote imaging spectroscopy of the Aliso Canyon CH4 superemitter, Geophysical Research Letters, 43, 6571–6578, doi:10.1002/ 2016GL069079, URL https://agupubs.onlinelibrary.wiley.com/doi/abs/10.1002/ 2016GL069079, 2016.

Thompson, D. R., Natraj, V., Green, R. O., Helmlinger, M. C., Gao, B.-C., and Eastwood, M. L.: Optimal estimation for imaging spectrometer atmospheric correction, Remote Sensing of Environment, 216, 355 – 373, doi:https://doi.org/10.1016/j.rse.2018.07.003, URL http: //www.sciencedirect.com/science/article/pii/S0034425718303304, 2018.

Thorpe, A. K., Frankenberg, C., and Roberts, D. A.: Retrieval techniques for airborne imaging of methane concentrations using high spatial and moderate spectral resolution: application to AVIRIS, Atmospheric Measurement Techniques, 7, 491–506, doi:10.5194/amt-7-491-2014, URL https://www.atmos-meas-tech.net/7/491/2014/, 2014.

Thorpe, A. K., Frankenberg, C., Green, R. O., Thompson, D. R., Aubrey, A. D., Mouroulis, P., Eastwood, M. L., and Matheou, G.: The Airborne Methane Plume Spectrometer (AMPS): Quantitative imaging of methane plumes in real time, in: 2016 IEEE Aerospace Conference, pp. 1–14, doi:10.1109/AERO.2016.7500756, 2016.

5   Thorpe, A. K., Frankenberg, C., Thompson, D. R., Duren, R. M., Aubrey, A. D., Bue, B. D., Green, R. O., Gerilowski, K., Krings, T., Borchardt, J., Kort, E. A., Sweeney, C., Conley, S., Roberts, D. A., and Dennison, P. E.: Airborne DOAS retrievals of methane, carbon dioxide, and water vapor concentrations at high spatial resolution: application to AVIRIS-NG, Atmospheric Measurement Techniques, 10, 3833–3850, doi:10.5194/amt-10-3833-2017, URL https://www.atmos-meas-tech.net/10/3833/2017/, 2017.

10 Turner, A. J., Jacob, D. J., Wecht, K. J., Maasakkers, J. D., Lundgren, E., Andrews, A. E., Biraud,
S. C., Boesch, H., Bowman, K. W., Deutscher, N. M., Dubey, M. K., Griffith, D. W. T., Hase, F., Kuze, A., Notholt, J., Ohyama, H., Parker, R., Payne, V. H., Sussmann, R., Sweeney, C., Velazco, V. A., Warneke, T., Wennberg, P. O., and Wunch, D.: Estimating global and North American methane emissions with high spatial resolution using GOSAT satellite data, Atmospheric Chemistry and Physics, 15, 7049–7069, doi:10.5194/acp-15-7049-2015, URL https://www.atmos-
15 chem-phys.net/15/7049/2015/, 2015.

Turner, A. J., Jacob, D. J., Benmergui, J., Brandman, J., White, L., and Randles, C. A.: Assessing the capability of different satellite observing configurations to resolve the distribution of methane emissions at kilometer scales, Atmospheric Chemistry and Physics, 18, 8265–8278, doi:10.5194/acp-18-8265-2018, URL https://www.atmos-chem-phys.net/18/8265/2018/, 2018.

20 Varon, D., Jacob, D., McKeever, J., Durak, B., and Jervis, D.: Quantifying Methane Emissions from Individual Coal Mine Vents with GHGSat-D Satellite Observations, in: AGU Fall Meeting Abstracts, 2018b.

Varon, D. J., Jacob, D. J., McKeever, J., Jervis, D., Durak, B. O. A., Xia, Y., and Huang, Y.: Quantifying methane point sources from fine-scale satellite observations of atmospheric methane plumes, Atmospheric Measurement Techniques, 11, 5673–5686, doi:10.5194/ amt-11-5673-2018, URL https://www.atmos-meas-tech.net/11/5673/2018/, 2018a.

25 Xi, X., Natraj, V., Shia, R. L., Luo, M., Zhang, Q., Newman, S., Sander, S. P., and Yung, Y. L.: Simulated retrievals for the remote sensing of CO2, CH4, CO, and H2O from geostationary orbit, Atmospheric Measurement Techniques, 8, 4817–4830, doi:10.5194/amt-8-4817-2015, URL https://www.atmos-meas-tech.net/8/4817/2015/, 2015.

Table 1. Shortwave infrared (SWIR) remote sensors for observing methane point sources

Instrument	Pixel size (km^2)	SWIR spectral range (nm)[a]	Spectral resolution (nm)[b]	Signal-to-noise ratio (SNR)[c]	Observing record
Aircraft					
AVIRIS-NG[d]	0.003×0.003	1600-1700; 2200–2510	5.0	200-400[e]	Campaigns
Satellite					
Atmospheric sensors					
SCIAMACHY[f]	30×60	1630–1670	1.4	1500	2002-2012
GOSAT[g]	10×10	1630–1700	0.06	300	2009-
GHGSat[h]	0.05×0.05	1600–1700	0.3–0.7[i]	N/A[j]	2016-
TROPOMI[k]	7×7	2305–2385	0.25	100	2017-
AMPS[l]	0.03×0.03	1990–2420	1.0	200-400	Concept
Imaging spectrometers					
PRISMA[m]	0.03×0.03	1600-1700; 2200–2500	10	180	2019-
EnMAP[n]	0.03×0.03	1600-1700; 2200–2450	10	180	2020-
EMIT[o]	0.06×0.06	1600-1700; 2200–2510	7–10	200-300	2022-
SBG[p]	0.03×0.03	1600-1700; 2200–2510	7–10	200-300	2025-
CHIME[q]	0.03×0.03	1600-1700; 2200–2510	<10	In preparation	2025-

[a]Methane has absorption bands around 1650 and 2300 nm (Figure 1).

[b]Spectral resolution is represented by the full-width at half-maximum (FWHM).

[c]For SCIAMACHY and GOSAT, SNR is for the CO_2 band used in the CO_2-proxy method retrieval. For other instruments, SNR is at 2300 nm. SNR estimates are for a reference 30° solar zenith angle and 0.3 surface reflectivity with clear sky.

[d]Airborne Visible/Infrared Imaging Spectrometer – Next Generation (Thorpe et al., 2017). AVIRIS-NG provides roughly a ground sampling distance (GSD) of 1 m per km altitude. The Frankenberg et al. (2016) and Duren et al. (2019) campaigns operated at 3-4 km altitude.

[e]Along-track oversampling increases SNR by $\sqrt{N}$ where N = number of along-track frames. AVIRIS-NG typically has $N > 4$ so AVIRIS-NG effective SNR at 2300 nm can be as much as 400.

[f]SCanning Imaging Absorption SpectroMeter for Atmospheric CHartographY (Frankenberg et al., 2006)

[g]TANSO-FTS instrument aboard the Greenhouse gases Observing SATellite (Kuze et al., 2016). Pixels are circles of 10 km diameter separated by about 250 km along track and cross-track.

[h]GreenHouse Gases Satellite (McKeever et al., 2017).

5   [i]GHGSat SNR is not comparable to other missions due to difference in instrument concept.

[j]Spectral resolution differs on the demonstration instrument GHGSat-D vs. upcoming missions GHGSat-C1,C2.

[k]TROPOspheric Monitoring Instrument (Hu et al., 2018)

[l]Airborne Methane Plume Spectrometer (Thorpe et al., 2016)

[m]PRecursore IperSpettrale della Missione Applicativa (http://prisma-i.it)

10   [n]Environmental Mapping and Analysis Program (Guanter et al., 2015)

[o]Earth Surface Mineral Dust Source Investigation (Green et al., 2018)

[p]Surface Biology and Geology, previously called HyspIRI (Hochberg et al., 2015)

[q]Copernicus Hyperspectral Imaging Mission For The Environment (Nieke and Rast, 2018)

Table 2. True and retrieved point source rates from EnMAP scene simulations with WRF-LES methane plumes.

Surface type[a]	True source rate ($kg\ h^{-1}$)[b]	Retrieved source rate ($kg\ h^{-1}$)[c,]
Grass	100	No plume detected
Grass	500	279 ± 101
Grass	900	542 ± 38
Urban	100	1080 ± 216
Urban	500	964 ± 198
Urban	900	1060 ± 134
Bright	100	93.5 ± 18.3
Bright	500	338 ± 83.1
Bright	900	577 ± 115

[a]Surface reflectances determined using the End-to-End Simulation Tool (EeteS; Figure 2)

[b]Prescribed in the WRF-LES methane plume simulations (Section 2)

5   [c]Mean and standard deviation of retrieved source rates for five WRF-LES plume realizations.
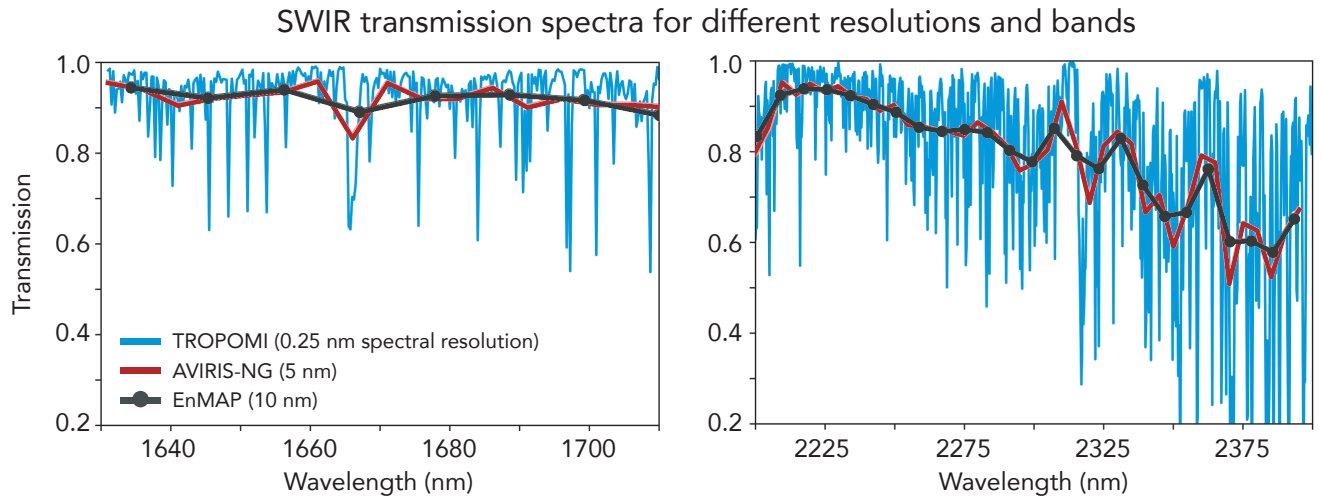
Figure 1. Simulated top of the atmosphere (TOA) transmission spectra for different spectral resolutions (FWHM = full-width at half-maximum) in the 1650 nm (left panel) and 2300 nm (right panel) shortwave infrared (SWIR) bands. High-resolution spectra were simulated for the U.S. Standard Atmosphere with 1800 ppb total column methane using the HITRAN 10 spectroscopic database and the HITRAN Application Programming Interface (HAPI) tool (Kochanov et al., 2016), and were then sampled with spectral resolutions of 0.25 nm (TROPOMI), 5 nm (AVIRIS-NG), and 10 nm (EnMAP) at the appropriate wavelength positions.
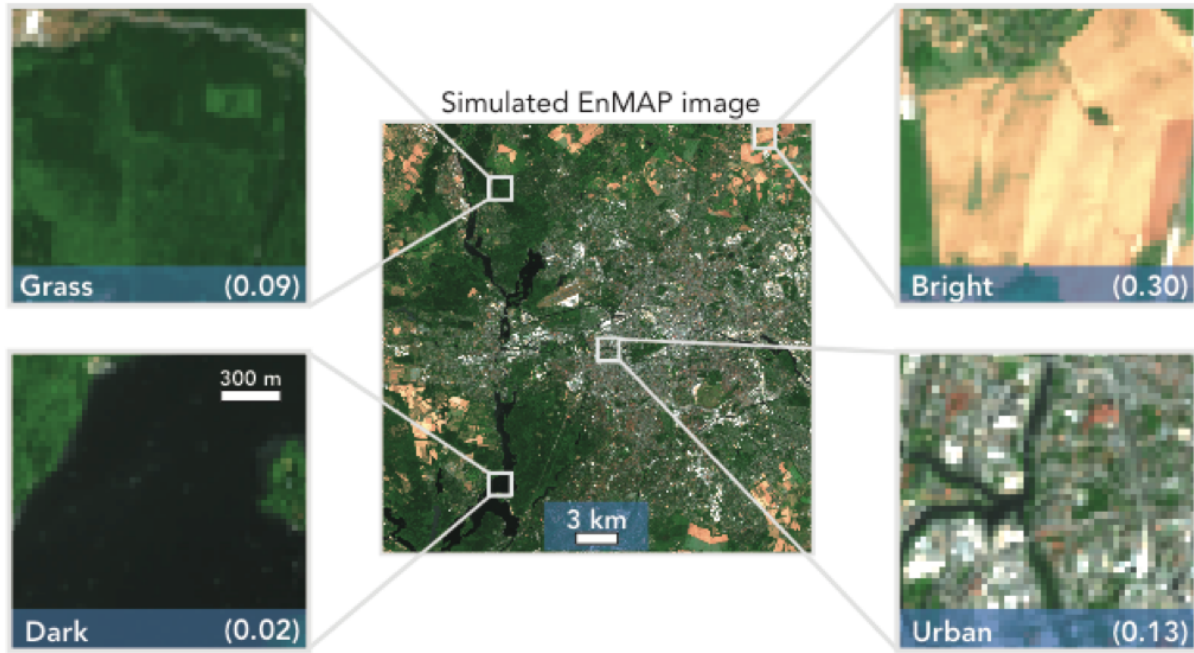
5 **Figure 2**. RGB image of a synthetic EnMAP scene simulated using the EnMAP End-to-End Simulation Tool (EetsS) over Berlin. Four scenes with 30×30 m^2 pixel resolution are shown (Grass, Dark, Bright, Urban) with average surface reflectances in the SWIR (2210-2410 nm) given in parentheses. These different scenes are used in Section 3 to evaluate the ability of EnMAP to retrieve atmospheric methane plumes.
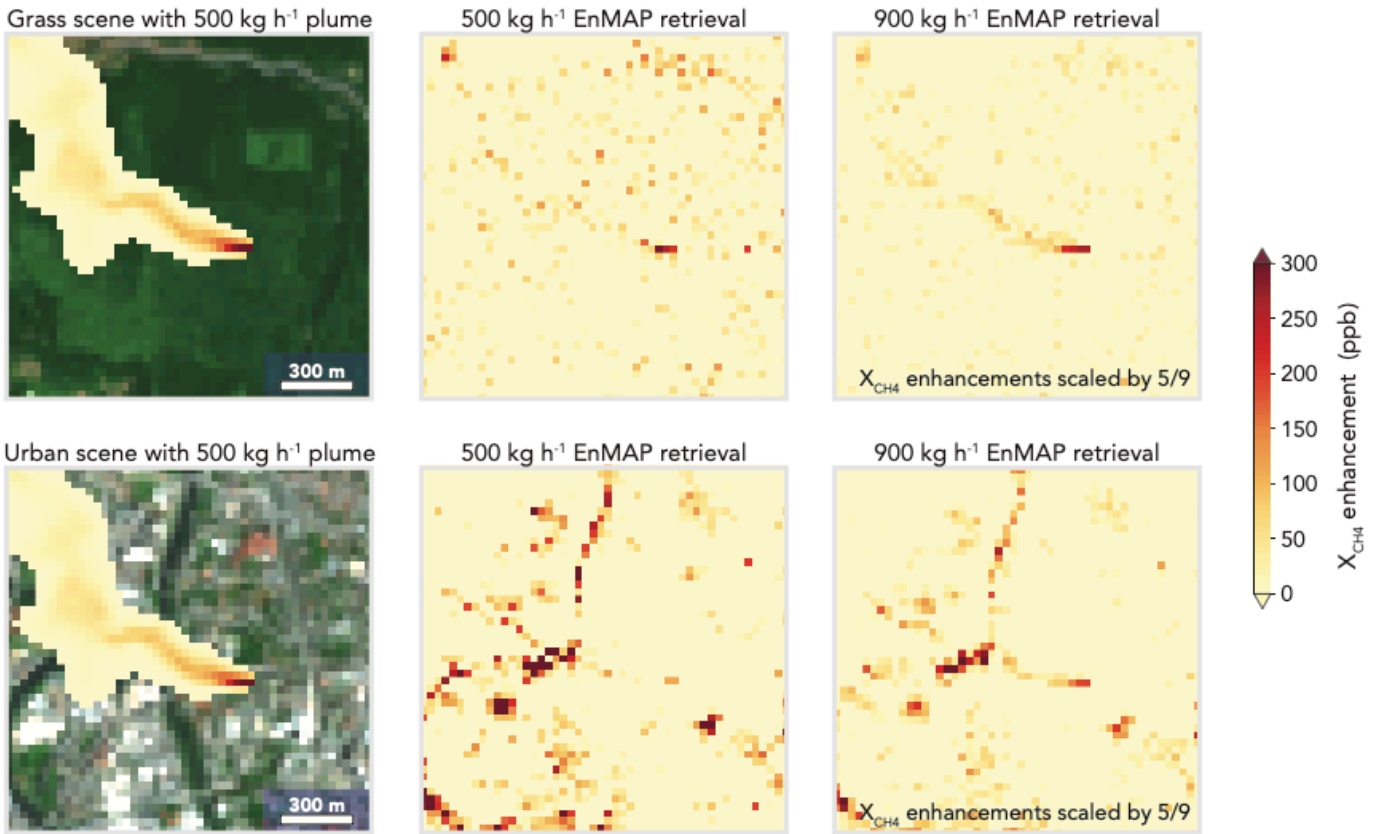
Figure 3. Retrieval of a methane plume over grass (top) and urban (bottom) EnMAP scenes. The plume was generated by WRF-LES at 30x30 m² resolution with a source rate of either 500 kg h⁻¹ or 900 kg h⁻¹. The left panels show the dry air column mixing ratio (X_{CH4}) enhancements relative to the 1800 ppb background for a 500 kg h⁻¹ methane plume superimposed on the RGB images of Figure 2. The middle panels show the retrieval of those enhancements using the IMAP-DOAS retrieval algorithm applied to the EnMAP instrument specifications. The right panels show the retrieval of the 900 kg h⁻¹ plume. The X_{CH4} enhancements in the right panels are scaled by 5/9 to be comparable with the other panels. Negative enhancements are reset to equal the background.
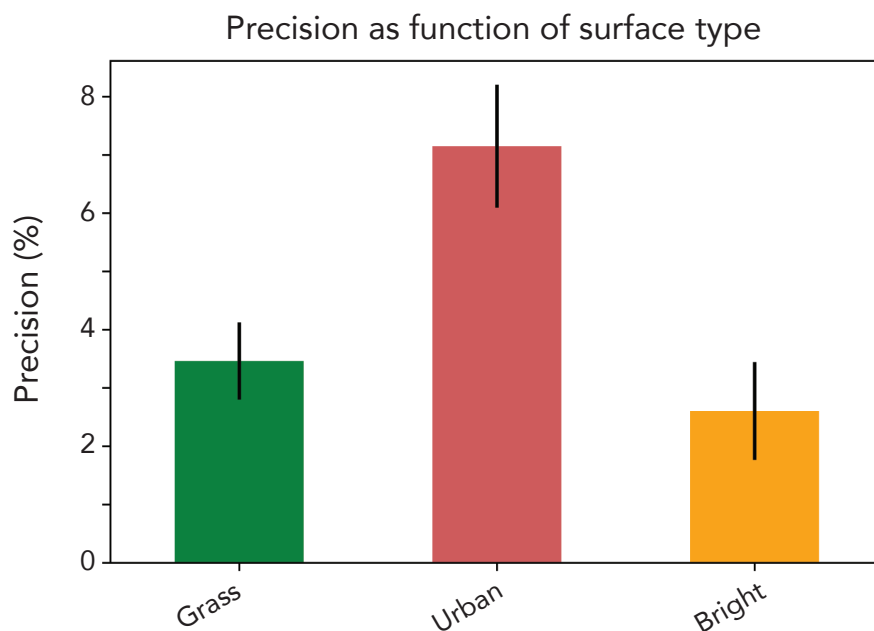
Figure 4. Precision of atmospheric methane retrievals from the EnMAP instrument (Table 1) over the Grass, Urban, and Bright surfaces of Figure 2. Precision is defined as the relative residual standard deviation (RRSD) between the "true" methane columns in synthetic scenes and values obtained from the IMAP-DOAS retrieval applied to the EnMAP top-of-atmosphere (TOA) backscattered radiances. The error bars represent the standard deviation over 15 WRF-LES plume realizations and 3 source magnitudes for the plume (100, 500, 900 kg h^{-1}). Precision over the Dark surface in Figure 2 is worse than 100%.
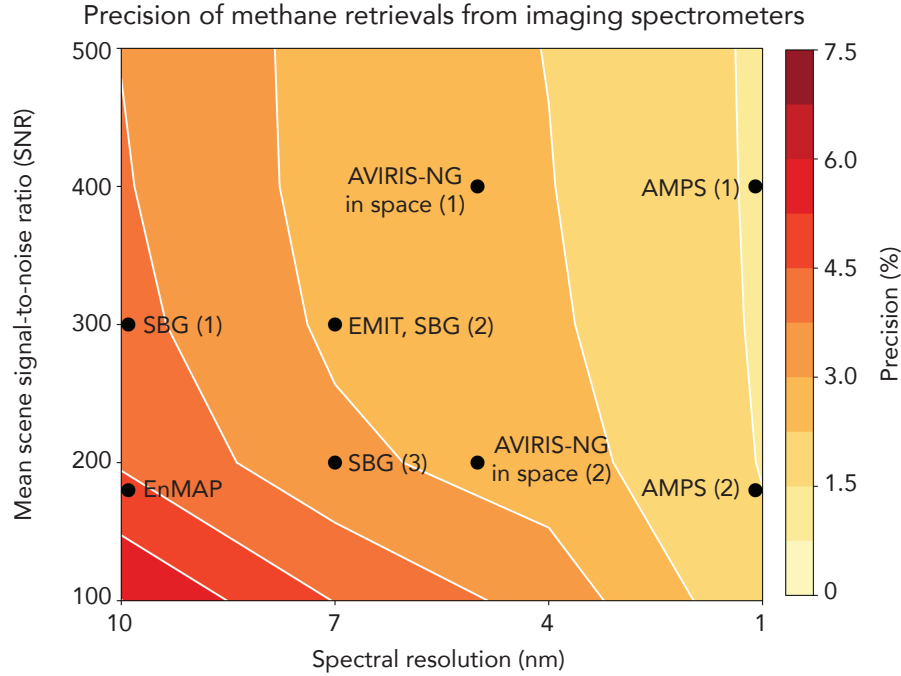
Figure 5. Precision of methane retrievals for spaceborne imaging spectrometers observing in the SWIR (2210-2400 nm), as a function of instrument signal-to-noise (SNR) and full-width half-maximum (FWHM) spectral resolution. The SNR values are for a reference 30° solar zenith angle and 0.3 surface reflectivity with clear sky, same as in Table 1. Actual SNR for individual pixels may vary, depending in particular on surface reflectivity. Precision is expressed as the relative residual standard deviation (RRSD) of the difference between retrieved and true methane columns over three synthetic scenes of Figure 2 (Grass, Urban, Bright) including point sources of 100-900 kg h^{-1} and for 15 different WRF-LES plume realizations. Black dots show different instrument specifications from Table 1. Specifications for the SBG and AMPS instruments are still at the design stage and values shown here are for the ranges under consideration. Results given for AVIRIS-NG are for a satellite instrument with 30×30 m[2] pixel resolution but other specifications (spectral resolution, SNR) same as the airborne instrument.

Plume pattern recognition for different instrument specifications
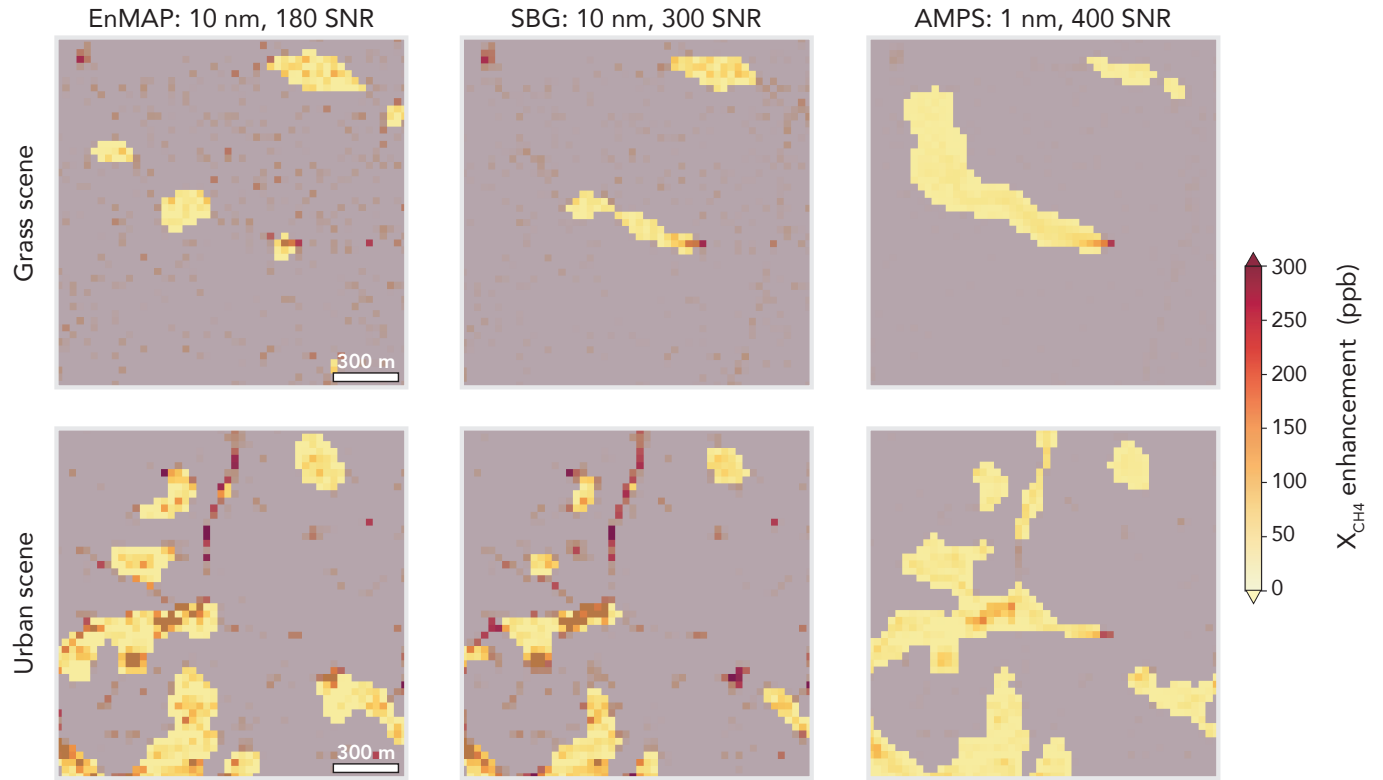
Figure 6. Plume pattern recognition algorithm applied to a point source of 500 kg h⁻¹ over Grass and Urban scenes as shown in Figure 3. The plume pattern is defined by applying median and Gaussian filters to pixels above the 80th percentile of X_{CH4} in the scene. Areas excluded by the mask are shown in gray. The panels show retrievals from the EnMAP, SBG, and AMPS instruments.

Methane retrievals over oil/gas facilities in California
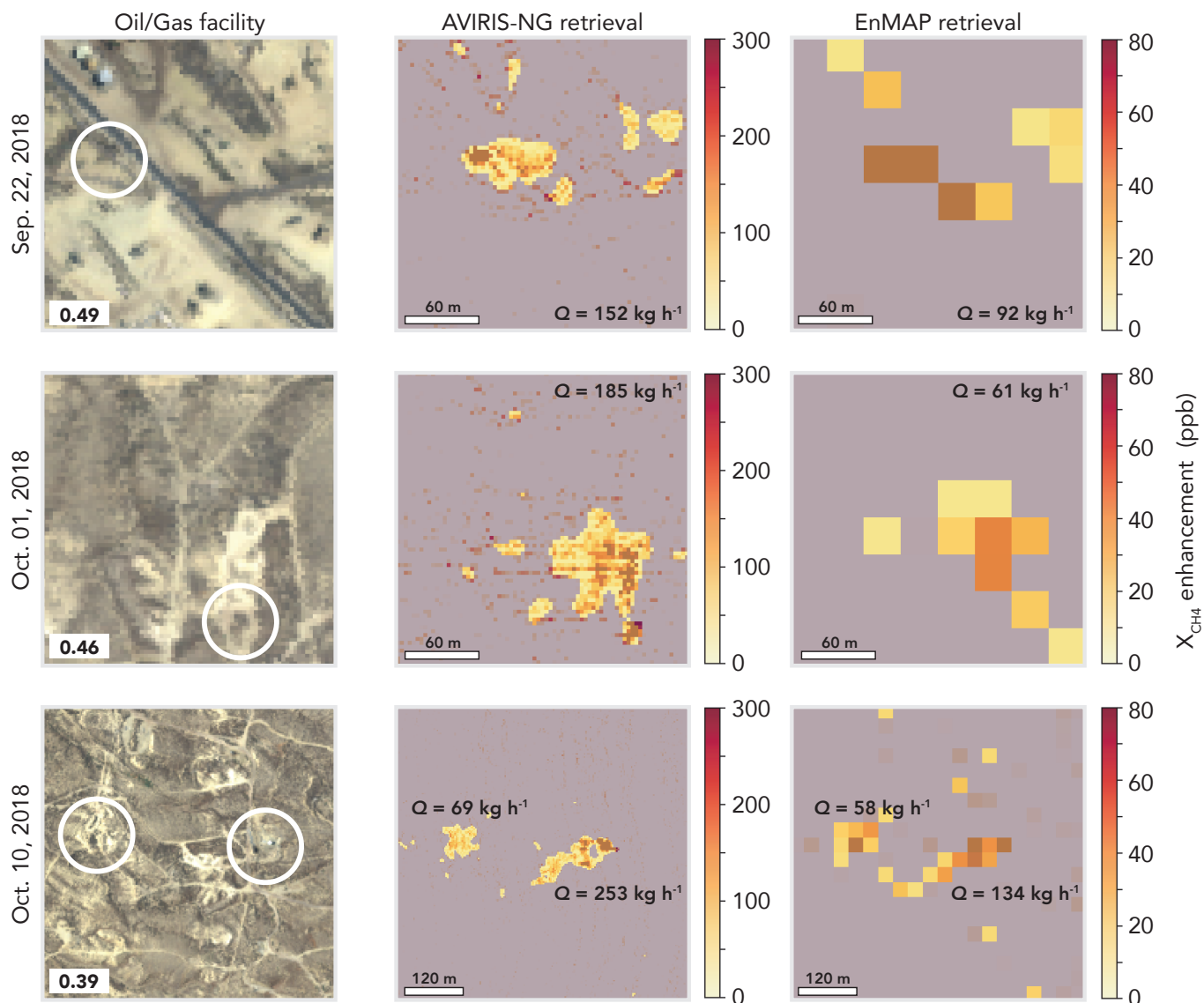
Figure 7. Retrieval of atmospheric methane plumes from facilities in the San Joaquin Valley of California imaged by the AVIRIS-NG instrument at 3-4 km altitude (CARB, 2017). The left panels show the RBG images mapped by AVIRIS-NG with the oil/gas facilities of interest circled. Inset in the bottom left corner is the mean retrieved SWIR surface reflectivity for the scene. The middle panels show the IMAP-DOAS retrieval applied to the AVIRIS-NG images with 3×3 m^2 pixel resolution and 5 nm spectral resolution. The right panels show the IMAP-DOAS retrieval applied to spectra that were spatially and

spectrally downsampled to match EnMAP instrument specifications (30×30 m^2 pixels, 10 nm spectral resolution). Note the difference in color scale for the methane enhancements in the AVIRIS-NG and EnMAP retrievals, reflecting the coarser pixel resolution of EnMAP. The plume mask described in the text is overlaid on each. The source rates for each plume obtained from the IME method are inset.